Drainage in a SL porous flowcell: Experimental and numerical studies

Dustin Crandall[a,b], Goodarz Ahmadi[a] and Duane H. Smith[b]

[a]Mechanical and Aeronautical Engineering Department Clarkson University, Potsdam NY USA 13699

[b]United States Department of Energy – National Energy Technology Laboratory, Morgantown WV USA 26505

Abstract:

A new flowcell has been designed and created using stereolithography (SL). This porous media geometry has been used for experimental and numerical studies of immiscible two-phase drainage. With SL construction both the throat heights and the throat widths have been varied. This has created a cell with a wide variability of throat properties. Additionally, a Volume of Fluid (VOF) of the same flowcell geometry has been studied. The experimental studies of air invading the flowcell saturated with water have shown a change from dendritic fingering structures to more stable displacements as the constant injection rate was reduced. This corresponds to a decreased fractal dimension and percent saturation of the invading air at low flow rates. The numerical model was first tested with the same fluids (air and water) and was shown to be in good agreement to the experiments. This VOF model was than extended to study different fluid-fluid pairings within the flowcell. As the defending fluid viscosity was increased the percent saturation of the invading fluid was shown to decrease. The SL construction has enabled the same geometry to be studied experimentally and numerically, thus allowing a wide variety of conditions to be analyzed.

Introduction:

An understanding of the displacement efficiency of two-phase flows in porous media is important in many engineering applications, including enhanced oil and gas recovery (Ahmed 2001, Jikich *et al.* 2003), dense non-aqueous liquid remediation of contaminated sites (Hwang *et al.* 2006), and geologic CO_2 sequestration (Holloway 2005). To study two-phase flows in porous media many experimental and numerical procedures have been used. A novel flowcell has been designed, constructed, and used for experimental

studies of two-phase drainage to extend upon this body of work. A finite-element Volume of Fluid (VOF) model has also been created with this geometry and the results show good agreement with the experimental results. With the numerical model various fluid-fluid conditions are shown to affect the percent saturation and fractal dimension (D_f) of the invading fluid, two characteristics related to the displacement efficiency.

Some of the first heterogeneous porous media models to be used in experimental studies were performed with glass/sand packs (Chuoke *et al.* 1959, Guckert & SanFillippo 1978). Packed beds are typically constructed from a pair of closely spaced glass or plastic plates, filled with beads or sand. With this, and similar devices, the interface between immiscible two-phase flows can be visualized with much greater ease than in geologic porous media. This, coupled with the fairly simple construction, has made studies in packed beds a desirable and practical alternative studying flow in rock (Bear 1972). As manufacturing processes have evolved the control of pore and throat geometries of experimental porous media models has improved.

Studies with etched cells were first described in the 1960's, and used with greater frequency in the 1980's. Etched cell production has become more refined over the past decades, as discussed in a review by Buckley (1991). Etched cells consist of a matrix of pores and throats, scribed into a base-plate, upon which a flat plate is attached. Variations of construction include glass etched cells created with photolithography (Theodoropoulou *et al.* 2003), glass cells with sandblasted pore-throat matrices (Ferer *et al.* 2004), resin cells etched with photolithography (Lenormand *et al.* 1988), and deep-reactive-ion-etching of micro-scale resin cells (Cubaud *et al.* 2006). These models have been used for analysis of pore-level, two-phase flow studies, under various conditions.

Etched cells have been used to study the dissolution of solutes in porous media (Theodoropoulou *et al.* 2003), the displacement characteristics of Newtonian and non-Newtonian fluids (Culligan *et al.* 2006, Perrin *et al.* 2006), and the effect of gravitational forces on immiscible flow (Ferer *et al.* 2004). The D_f of the invading fluid mass has also been evaluated in many experimental studies. Fractals are non-Euclidian structures that are well described by a power relationship, related to the D_f; in-depth discussions of fractals can be found in the books by Mandelbrot (1983) and Feder (1988). The D_f of

invading fluid fingers are typically shown to change as flow and fluid-fluid properties are varied.

The viscosity ratio (M) is an important fluid-fluid parameter in two-phase flow through porous media. The M is the ratio of the invading fluid absolute viscosity ($_{inv}$) to the defending fluid's viscosity ($_{def}$), ie.

$$M = \frac{\mu_{inv}}{\mu_{def}} \tag{1}$$

M > 1 indicates stable displacement in porous media (Ferer *et al.* 2007), while M<1 indicates unstable displacement (fingering). As M decreases the fingering structures have been shown to become more dendritic in both numerical (Ferer *et al.* 2003) and experimental (Lenormand *et al.* 1988) studies. For this study only unstable viscosity ratios (M < 1) are studied.

The capillary number (Ca) of the flow, which is the ratio of viscous forces to the surface tension forces, is defined as

$$Ca = \frac{\mu_{def} U}{c \cos\theta} \tag{2}$$

here U is the mean velocity through the flowcell, is the interfacial tension coefficient between fluids and is the static contact angle between the cell boundaries and the defending fluid. As the Ca increases the fingering of the invading fluid has been shown to become more dendritic, and likewise lower Ca are associated with more stable displacements (Lenormand *et al.* 1988).

Numerical models of two-phase flow through porous media have been conducted by numerous investigators over the past decades; a review by Blunt (2001) discusses many of these works. By far, the most common numerical tool used in these analyses has been pore-throat models. A pore-throat model of two-phase fluid motion solves the pressure field in a random matrix of connected pores and throats, calculates the resistances in each throat due to capillary and viscous relationships, and moves the invading fluid through the throat with the least resistance (Ferer *et al.* 2003). Numerous variations on this technique have been used, including models with different throat distributions (Stevenson *et al.* 2006), radial models (Chen & Wilkinson 1985) and models

that include various body forces, such as gravity (Ferer *et al.* 2004). The relative speed of these models has enabled the study of large matrices, with 250 million pore systems modeled in some studies (Ferer *et al.* 2007).

Other numerical methods have been used to study two-phase flow in porous media. A simpler, stochastic pore level model which does not solve the pressure field was presented by Paterson *et al.* (1996), a localized Darcy's law has been used to solve flow through idealized fractures by Saghir *et al.* (2000), with mediocre results. Fast, first order approximations to two-phase flow through porous media was solved with a novel numerical/electrical analogy by Aumeerally & Sitte (2006). The comparison of these models has been, for the most part, qualitative.

The present numerical modeling was done with the finite element, computational fluid dynamics software FLUENT^{TM}. Similar finite element models of porous media have been used previously to model single phase flow in flowcells. Work by Andrade Jr. *et al.* (1999) and Mazaheri *et al.* (2005) have shown the change from flows that are well predicted by Darcy's Law to flows which are dominated by inertial forces. A single phase finite element model was used by Perrin et al. (2006) to compare to experimental Newtonian and non-Newtonian flows. No two-phase finite element models in flowcells has been identified in the literature. A two-phase finite element model of viscous fingering in a Hele-Shaw cell presented by Nakayama and Motogami (1998) is similar to the work presented here, with simpler set of boundary conditions and a smaller number of computational grid elements.

Code was developed in-house to design the new flowcell which was then constructed using stereolithography (SL). With SL, a wide range of flowcell throat geometries pertinent to two phase flow resistances encountered in flow through porous media was created. With this cell a large range of Ca values have been experimentally studied for the case of air invading a water saturated cell, $M = 1.8(10^{-2})$.

Flowcell Construction and Properties

Experimental studies of two-phase flow in porous media analogies have been performed with increasingly complex models over the past half of a century (Buckley 1991, Blunt 2001). The flowcell used for this study was created with SL at Clarkson

University (Leonard 2007). In SL production a laser cures a thin layer of photo-sensitive resin on the surface of a vat of liquid resin, a movable platform then submerges the cured layer and a new layer is cured on top of the previous one (Nee *et al.* 2001). The use of this type of production has two distinct advantages; (1) the same geometry can be used for numerical and experimental studies (2) the height of each throat/pore can be varied, due to the 'bottom-up' layered construction. Thus SL production was able to produce a flowcell with a wider range of throat areas and perimeters, which are related to the individual throat capillary resistances and transmissivities.

The flowcell was created from an in-house C++ code which generated a uniform distribution of 5200 throat widths (w_t), 0.35mm < w_t < 1.0mm (0.014 in < w_t < 0.039 in), and randomly placed them within the 10.16 cm (4 in) square matrix. The cumulative distribution of the w_t's is shown in Figure 1(a). This primary code generated a Visual-LISP script to read into AutoCAD^{TM} and a three-dimensional computer model was automatically constructed. The throat heights (h_t) were varied with an ancillary piece of code. Seven separate h_t, from 0.2mm to 0.8mm (0.008 in to 0.031 in), were assigned to throats within the uniform interconnected w_t matrix, with the smallest w_t throats assigned the smallest h_t and the largest w_t the largest h_t. The 'pores' (where the throats intersect) were set to the mean h_t, 0.5mm (0.02 in). The flowcell matrix is shown in Figure 1(b), with cross-sections of the matrix shown in Figure 1(c). The height of the cross-sections has been increased to show the variation in the pore/throat height.

The flowcell was manufactured with Clarkson University's SL machining capabilities on a 12.7 cm by 15.24 cm (5 in by 6 in) sheet of glass with 1.27 cm ($^1/_2$ in) ramped manifolds. The UV cured, translucent, and water resistant SL resin used was Accura SI-10. As shown in Figure 2, the flow cell geometry was surrounded by 1.27 cm ($^1/_2$ in) of SL resin. Two 3.175 cm ($^1/_8$ in) OD centered inlet/outlet tubes were added to complete the base. An equal sized, resin coated glass sheet was adhered to the top of the base geometry. A small amount of resin was spread over the base geometry, the two flowcell halves were pressed together, and cured under UV light to initially adhere the sides. Finally, quick-set epoxy was added to the perimeter of the cell to create the finished cell. This cell is shown in the upper right insert in Figure 2.

The static contact angle ( ) of the water-air-resin interface was measured as $72^{o}\pm2$ with a Data Physics Contact Measurement System and the G-contact method (Richards 2006). All reported in this paper were measured through the defending fluid, water. The resin differs from glass, where $0^{o} < 25^{o}$, depending on the cleanliness of the glass. The porosity of the cell was calculated as 37.2%, as defined by ratio of the open matrix volume (throats and pores) and the minimum surrounding volume which would completely surround the matrix.

As previously mentioned, both the h_t and w_t were varied to produce a wider range of throat properties. The individual capillary resistance of each throat (P_c) is dependant on the radii of the invading meniscus. For a square flowcell throat P_c is given as

$$P_c = 2\sigma\cos\theta\left(1/h_t + 1/w_t\right) \tag{3}$$

Here the meniscus radii are assumed to be equal to half the w_t and h_t. To compare the current SL flowcell throat variability to other cells the ratio of smallest to largest throat ($1/h_t+1/w_t$) for the current cell, the glass cell used in Ferer *et al.* (2004) and the current cell w_t distribution with h_t = 0.5 mm (0.02 in) are tabulated in Table 1.

The transmissivity of a throat (g_t) is a parameter which describes the viscous resistance to fluid motion due to restricted throat area, and is given as

$$g_t = G\frac{(A_t)^2}{t_l^4\left(x-(1-x)\right)M} \tag{4}$$

where G is a geometric constant, t_l is the throat length, and x is the percent of the throat the invading fluid has penetrated. To compare the current SL flowcell g_t range to other cells, the ratio of $(A_t)^2$ for the current cell, the glass cell used in Ferer *et al.* (2004) and the current cell w_t distribution with h_t = 0.5 mm (0.02 in) are tabulated in Table 2.

As can be seen, the new SL flowcell has a wider range of geometric throat properties pertinent to P_c and g_t resistances, as compared to similar cells with no h_t variation.

Experimental Modeling

The experimental setup consisted of a constant rate syringe pump (KD Scientifc KDS 200) that was used to control the injection of air into the horizontal, water-saturated

flowcell. A CCD camera (NTSC COHU 4915-400/000) was used to capture the images. The pressure across the cell was measured at the same time images were recorded by a pressure transducer (Setra C239). The acquisition and storage of this data was controlled by a LabView module and manufacturer provided scripts. A schematic of this setup is shown in Figure 3. This experimental setup is nearly identical to that described by Ferer *et al.* (2004). All experiments were performed with a horizontal flowcell and air injection into a water saturated flowcell. Percent saturations were measured at the "breakthrough" time, when the air reached the end of the flowcell matrix.

The captured black and white images were post-processed to determine the percent saturation and D_f, as measured by box-counting, of the invading air. This permitted a comparison to prior studies and provided a means to verify the accuracy of the current numerical models. To remove glare and lighting inconsistencies an image of the cell prior to air invasion was subtracted from the breakthrough image. This merged image was then cropped to include only the square matrix and rotated so that the flow was bottom to top. The image was enhanced to make the invaded regions the brightest and a threshold was applied to isolate the portion of the matrix which had been invaded by air. This image processing was performed with the Gnu Image Manipulation Program (GIMP 2007) and saved as an 8-bit black and white bitmap.

The percent saturation of the area filled with air and D_f was measured with ImageJ (2007). The invading air saturation profile was not observed to change significantly after the air broke through the matrix, regardless of the flow rate. This is different from previous studies (Ferer *et al.* 2004) and believed to be due to the increased contact angle, as compared to glass-air-water interfaces.

Experiments of air injection into a flowcell saturated with water were performed. The constant injection rate was varied from 20 $^{ml}/_{min}$ to 0.02 $^{ml}/_{min}$, corresponding to Ca of $9(10^{-4})$ to $9(10^{-7})$. For experimental Ca calculations the Darcy velocity, V_{Darcy} (Hansen 2003) was used as the mean velocity (U) in Eqn. (2) and is given as

$$V_{Darcy} = \frac{Q}{A_{cell}} \tag{5}$$

Here Q is the constant volume injection rate and A_{cell} is the cross-sectional area of the flowcell, perpendicular to the mean flow direction. Over this range of flow rates the fingering patterns were shown to vary from dendritic fingers to more stable displacement patterns.

Numerical Modeling

FLUENT^{TM} was used to solve the Navier-Stokes equations on an unstructured finite element grid within the flowcell geometry. The VOF model calculates the volume fraction ($_j$) of each fluid in a cell within the computational domain

$$\frac{1}{\alpha_j}\left[\frac{\partial}{\partial t}(\alpha_j \rho_j) + \nabla \bullet (\alpha_j \rho_j \vec{u}_j)\right] = 0 \tag{6}$$

where $_j$ is the density and $\vec{u}_j$ is the velocity of the fluid j. This formulation is valid for immiscible two-phase flows with no source terms (FLUENT^{TM} 2005). Local (cell) averaged fluid properties ($\rho = \sum \alpha_j \rho_j \quad \mu = \sum \alpha_j \mu_j$) were calculated using the and the unsteady, variable density conservation of mass

$$\frac{\partial \rho}{\partial t} + \nabla g(\rho \vec{u}) = 0 \tag{7}$$

and conservation of momentum

$$\frac{\partial \rho \vec{u}}{\partial t} + \nabla g(\rho \vec{u}\vec{u}) = -\nabla P + \mu \nabla^2 \vec{u} + \rho \vec{g} + \vec{F} \tag{8}$$

were solved. In Eqns. (7) and (8) the fluid properties reflect the local averaging of Eqn. (6) and the force $\vec{F}$ is a volume force to account for interfacial forces. In this manner, a continuous solution for the case of zero mass transfer between fluids was obtained, with the density and pressure jump at the interface accounted for.

The interfacial tension between fluids was modeled as a volume force, after work by Brackbill *et al.* (1992), through an application of the divergence theorem on the surface force. From the gradient of $_j$ the surface normal, n, was calculated and the curvature of the interface was determined from the unit normal, $\hat{n}$. i.e.,

$$n = \nabla \alpha_j \quad \kappa = \nabla \cdot \hat{n} = \nabla \cdot \frac{n}{|n|} \tag{9}$$

Recognizing that for a two-phase system the = - j, the interfacial tension volume force was represented as

$$\vec{F} = \sigma_{ij} \frac{\rho \kappa_i \nabla \alpha_j}{\frac{1}{2}\left(\rho_i + \rho_j\right)} \tag{10}$$

Wall adhesion was also modeled using a method described in Brackbill *et al.* (1992). A static contact angle was defined for fluid-fluid-solid interfaces and this angle is permitted to be adjusted during computations. This temporal treatment accounts for the hysteresis observed between wetting fluid invasion and wetting fluid retreat.

As discussed by Nakayama & Motogami (1998), the computational accuracy of the surface tension calculations is highly dependant on the of the interface. And, in turn, is highly dependant on the mesh resolution used. For this reason, and to reduce the numerical diffusion between fluids, a highly refined mesh was required. A mesh of ~950,000 grid elements (545,000 nodes) was used. This corresponds to a minimum of four elements across each of the throats and was shown to nearly eliminate the numerical diffusion between the immiscible fluids.

Experimental Results

A minimum of three trials for each flow rate and through each side were performed; a total of 86 trials were conducted. Representative breakthrough images of flow from side 1 to side 2 are shown in Figure 4 for $9(10^{-4}) < Ca < 2.3(10^{-6})$. Breakthrough images from side 2 to 1 are shown for the same flow rates in Figure 5. It is readily apparent from these images that the saturation of the invading air increased with the lower Ca. Here, the black and white images in Figures 4 and 5 have been inverted for easier viewing.

The saturation of the invading air after breakthrough was calculated for all runs and averaged for each Ca. These results are presented in Figure 6, along with the reported values from the horizontal flowcell work from Ferer *et al.* (2004) (note Ca values from

the glass flowcell of Ferer *et al.* (2004) have been recalculated using Eqn. (2) and a of 15^{o}). The difference in is believed to be the primary reason for the increased percent saturation values from the current cell. Wetting characteristics have been shown to similarly affect the fingering patterns observed in a variation of the standard numerical pore-throat model by Koiler *et al.* (1992).

The D_f of the invading air mass was measured using a box-counting routine (ImageJ 2007). As shown in Figure 7, the fractal dimension of the air increases as the Ca decreases. This is consistent with prior experimental and numerical studies of drainage in flowcells (Ferer *et al.* 2004). The traditional D_f range for fingering in porous media is from 1.71 to 1.86, corresponding to the limits of diffuse limited aggregation and invasion percolation, respectively (Ferer *et al.* 2003). The D_f measured from the current experimental work was consistently lower than these values, though the increase from low D_f to higher D_f as the Ca decreased was observed. The discrepancy is believed to be due to the fairly high (72^{o}) of the SL flowcell. Most numerical models have assumed ~0 and many of the reported experimental work has been performed with low , glass flowcells.

Numerical Results

Numerical simulations using FLUENT^{TM} and the previously discussed VOF method were performed with a two-dimensional slice of the flowcell geometry used for experimental work. In this 10.16 cm (4 in) square domain ~950,000 unstructured grid elements were created with the pre-processing software GAMBIT^{TM}. Through progressive grid refinements, this mesh was found to nearly eliminate numerical diffusion at the interface and attain the proper at the fluid-fluid-solid interface.

The large number of numerical cells, unsteady solution and VOF modelling combined to make simulations that were computationally expensive. The majority of numerical flowcell models presented were performed on a minimum of 6 parallel processors over periods of up to three months. When contrasted with the speed of pore-throat models this is an incredibly expensive procedure and partially explains the lack of prior two-phase finite element flowcell studies in the literature.

A constant velocity inlet was specified, through which the invading fluid was injected. The magnitude of this velocity was varied to model different Ca flows. The outlet boundary condition was specified as a constant pressure outlet, at atmospheric pressure. An isothermal condition was assumed, thus the energy equation was not solved. These conditions were used to provide a direct comparison to experimental analyses.

A numerical simulation of air injection into the flowcell geometry, initially saturated with water (M=1.8(10^{-2})) and with = 72^{o} was first performed. The saturation of the air at breakthrough is shown in Figure 8. A constant injection velocity of $1^{cm}/_{s}$ was used and the resulting Ca = 4.5(10^{-4}), as determined from Eqn. (2). The percent saturation of the invading air was measured as 23.2%, with a user-defined function in FLUENT^{TM}, at breakthrough. The D_f was measured as 1.62 using the same procedure described in the experimental section (ImageJ 2007). The percent saturation value is in good agreement to the experimental studies, as shown in Figure 6. The D_f is lower than that measured in the experimental studies. The use of a mass-averaged length scale to determine the D_f has been shown to provide more accurate estimates by Ferer *et al.* (2004).

The fluid properties were than changed to represent air invasion into an oil saturated flowcell (M=1.7(10^{-5})). The was reduced to 35 $^{dynes}/_{cm}$ while the and inlet velocity were kept the same as the previously described model. As shown in Figure 9 this change in fluid properties produced a more dendritic fingering structure. The Ca of this flow was determined to be 0.98, much higher than the air into water simulation. The percent saturation of the invading air was measured as 10.1%, lower than the experimentally observed saturations. The D_f of the flow was measured as 1.51, lower than the air into water simulation and well below other published D_f values. This simulation was performed with a much higher Ca flow than has been typically been discussed in the literature. This high Ca partially explains the very low percent saturation and D_f values.

Discussion

A new SL flowcell has been designed, constructed and used for experimental studies of two-phase immiscible drainage in porous media. The computer generated geometry

created for this was also used in a finite element VOF series of simulations, with varying fluid properties. The use of the physical model geometry in the numerical simulations allows for direct comparisons between the two studies to be made, a situation which is not always possible with other numerical models. This increased numerical modeling capability comes at a cost; the numerical models are more computationally expensive than the majority of models discussed in the literature. Regardless of this cost, the use of finite element modeling within flowcells can extend the relevancy of previous pore level modeling to situations that are more pertinent to flow within actual reservoirs.

Conclusions

The new variable height stereolithography model can be used to examine a wide range of fingering types.

Experimental results show an increase in the percent saturation for the same Ca and M, as compared to studies with a lower .

Numerical FLUENT^{TM} VOF simulations are shown to accurately capture the interface evolution during constant rate injections in the complex flowcell geometry.

Numerical modelling of the flowcell geometry can be used to study situations which are difficult or impossible to study with the experimental model.

Experimental and numerical results show an increase in the invading fluid saturation at lower Ca values.

Acknowledgements
Gratitude to the USDOE National Energy Technology Laboratory, Morgantown WV is acknowledged for financial support of this work.

References:

Ahmed, T. Reservoir Engineering Handbook, 2nd ed., Gulf Professional Publishing, Houston, TX (2001)

Andrade, Jr., J.S., Costa, U.M.S., Almeida, M.P., Makse, H.A. & Stanley, H.E. Inertial effects on fluid flow through disordered media, Phys. Rev. Lett., Vol. 82, No. 26, 5249 – 5252 (June 1999)

Aumeerally, M. & Sitte, R. Layered fluid model and flow simulation for microchannels using electrical networks, Sim. Model. Prac. Theory, Vol 14, 82 – 94 (2006)

Bear, J. Dynamics of Fluids in Porous Media, Dover Publishing, New York, pp. 678-687 (1972).

Blunt, M.J. Flow in porous media – pore-network models and multiphase flow, Curr.

Opin. Colloid Interface Sci., Vol. 6, 187 – 207 (2001)

Brackbill, J.U., Kothe, D.B. & Zemach, C. A continuum method for modeling surface tension, J. Comput. Physics, Vol. 100, 335 – 354 (1992)

Buckley, J.S. Multiphase displacements in micromodels. In Interfacial Phenomena, no. 36 Surfactant Science Series, ed. Morrow, N.R. Marcel Dekker, Inc., New York (1991)

Chen, J.D. & Wilkensen, D. Pore-scale viscous fingering in porous media, Phys. Rev. Let. Vol. 55, No. 18, 1892 – 1895 (1985)

Chuoke, R.L., van Meurs, P. & van der Poel, C. The instability of slow, immiscible, viscous liquid-liquid displacements in permeable media, Petrol. Trans., Vol. 216, 188 – 194 (1959)

Cubuad, T., Ulmanella, U. & Ho, C.-M. Two-phase flow in microchannels with surface modifications, Fluid Dyn. Res., Vol. 38, 772 – 786 (2006)

Culligan, K.A., Wildenschild, D., Christensen, B.S.B., Gray, W.G. & Rivers, M.L. Pore-scale characteristics of multiphase flow in porous media: A comparison of air-water and oil-water experiments, Adv. Water Res., Vol. 29, 227 – 238 (2006)

Feder, J. Fractals, Plenum Press, New York (1988).

Ferer, M., Bromhal, G.S. & Smith, D.H. Pore-level modelling of immiscible drainage: validation in the invasion percolation and DLA limits, Physica A, Vol. 319, 11 – 35 (2003)

Ferer, M., Ji, C., Bromhal, G.S., Cook, J., Ahmadi, G and Smith, D.H. Crossover from capillary fingering to viscous fingering for immiscible unstable flow: Experiment and modelling, Phys. Rev. E., Vol. 70, 1-7 (2004)

Ferer, M., Bromhal, G.S. & Smith, D.H. Crossover from capillary fingering to compact invasion for two-phase drainage with stable viscosity ratios, Adv. Wat. Res., Vol. 30, 284 – 299 (2007)

FLUENT^{TM}, FLUENT 6.2. User's Manual, Lebanon, NH (2005)

GIMP, GNU Image Manipulation Program Manual, www.gimp.org (2007)

Guckert, L.G. & SanFillippo, G.P. Oil recovery by carbon dioxide injection. Tech. Report ORO-5301-34, U.S. Dept. of Energy (Sept. 1978)

Hansen, D. A review of terminology pertaining to Darcy's law and flow through porous media, J. Porous Media, Vol. 6, No. 2, 83 – 97 (2003)

Holloway, S. Underground sequestration of carbon dioxide – a viable greenhouse gas mitigation option, Energy, Vol. 30, 2318 – 2333 (2005)

Il Hwang, S., Pyo Lee, K., Soo Lee, D. and Powers, S.E. Effects of fractional wettability on capillary pressure-saturation-relative permeability relations of two-phase systems, Adv. Wat. Res., Vol. 29, 212 – 226 (2006)

ImageJ, ImageJ Version 1.24o Documentation, http://rsb.info.nih.gov/ij/docs/index.html (2007)

Jikich, S.A., Smith, D.H., Sams, W.N. & Bromhal, G.S. Enhanced gas recovery (EGR) with carbon dioxide sequestration: A simulation study of effects of injection strategy and operational parameters, SPE 84813, Presented at SPE Eastern Regional, Pittsburgh PA, USA (Sept. 2003)

Koiler, B., Ji, H. & Robbins, M.O. Fluid wetting properties and the invasion of square networks, Phys. Rev. B, Vol. 45, No. 14, 7762 – 7767 (April 1992)

Lenormand, R., Touboul, E. & Zarcone, C. Numerical models and experiments on immiscible displacements in porous media, J. of Fluid Mech., Vol. 189, 165 – 187 (1988)

Leonard, D. Stereolithography prototypes, http://www.clarkson.edu/rapidprototype/ (2007)

Mandelbrot, B. The fractal geometry of nature, W.H. Freeman & Co., New York (1983)

Mazaheri, A.R., Zerai, B., Ahmadi, G., Kadambi, J.R., Saylor, B.Z., Oliver, M., Bromhal, G.S. & Smith, D.H. Computer simulation of flow through a lattice flow-cell model, Adv. Water Res., Vol. 28, 1267 – 1279 (2005)

Nakayama, T. & Motogami, S. A finite element approach to the numerical computation of viscous fingering phenomena, Fluid Dynam. Res., Vol. 22, 73 – 87 (1998)

Nee, A.Y.C., Fuh, J.Y.H. & Miyazawa, T. On the improvement of the stereolithography (SL) process, J. Mat. Proc. Tech., Vol. 113, 262 – 268 (2001)

Paterson, L., Painter, S., Knackstedt, M.A. & Pinczewski, W.V., Patterns of fluid flow in naturally heterogeneous rocks, Physica A, Vol. 233, 619 – 628 (1996)

Perrin, C.L., Tardy, P.M.J., Sorbie, K.S. & Crawshaw, J.C. Experimental and modelling study of Newtonian and non-Newtonian fluid flow in pore network micromodels, J. Coll. Interface Sci., Vol. 295, 542 – 550 (2006)

Richards, M. Multiphase flow through porous media with applications to CO_2 sequestration, Masters Thesis, Clarkson University (2006)

Saghir, M.Z., Chaalal, O. & Islam, M.R., Numerical and experimental modelling of viscous fingering during liquid-liquid miscible displacement, J. Pet. Sci. Eng., Vol. 26, 253 – 262 (2000)

Stevenson, K., Ferer, M., Bromhal, G.S., Gump, J., Wilder, J. & Smith, D.S. 2-D network model simulations of miscible two-phase flow displacements in porous media: Effects of heterogeneity and viscosity, Physica A, Vol. 367, 7 – 24 (2006)

Theodoropoulou, M.A., Karoutsos, V., Kaspiris, C. & Tsakiroglou, C.D. A new visualization technique for the study of solute dispersion in a model porous media, J. Hydro., Vol. 274, 176 – 197 (2003)

Tryggvason, G. & Aref, H. Finger-interaction mechanisms in stratified Hele-Shaw flow, J. Fluid Mech., Vol. 154, 287 – 301 (1985)

$(1/w_t + 1/h_t)$	Smallest Throat	Largest Throat	Smallest/Largest
Glass cell (Ferer et al. 2004)	13.3	10	1.33
SL cell with $h_t = 0.5$mm	4.86	3	1.62
Constructed SL cell	7.86	2.25	3.49

Table 1: Ratio of throat properties related to capillary resistances.

$(A_t)^2$	Smallest Throat	Largest Throat	Largest/Smallest
Glass cell (Ferer *et al.* 2004)	$5.76(10^{-4})$	$5.18(10^{-3})$	9
SL cell with $h_t = 0.5$mm	$3.06(10^{-2})$	0.25	8.2
Constructed SL cell	$4.90(10^{-4})$	0.64	1300

Table 2: Ratio of throat properties related to throat transmissivity.

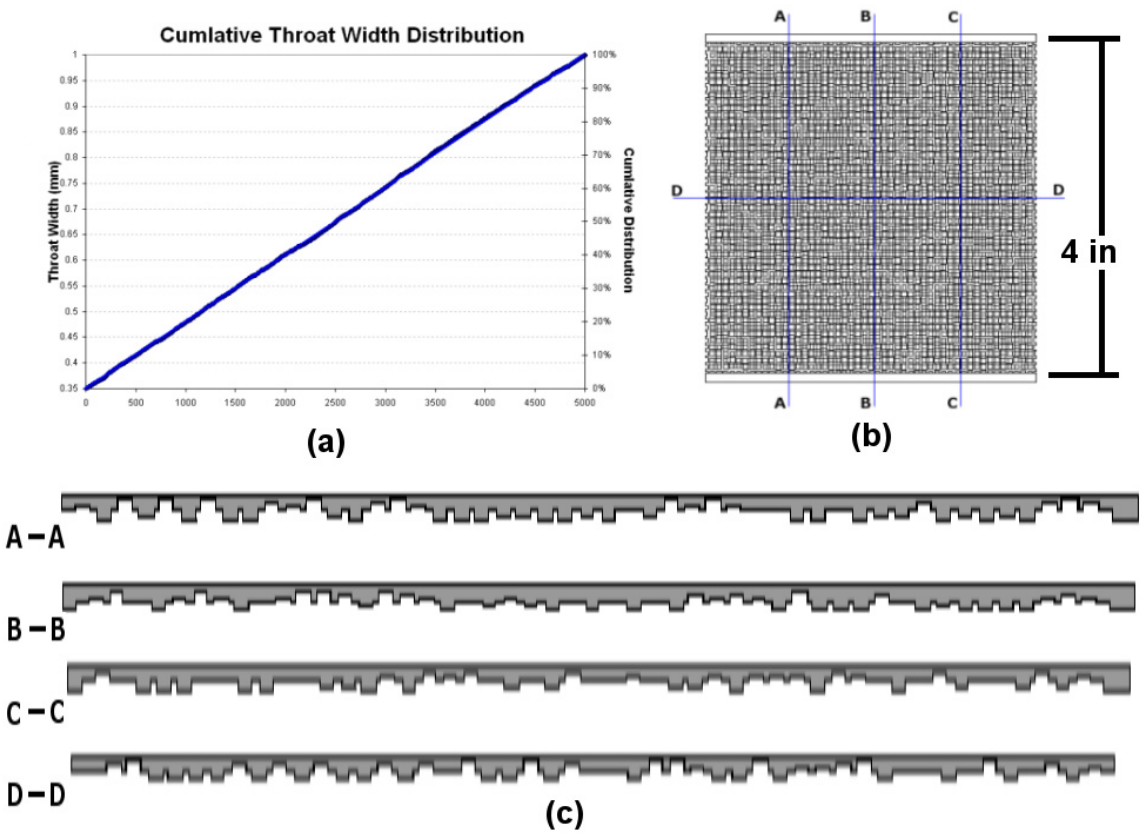

Figure 1: (a) Cumulative throat width distribution. (b) Flowcell matrix. (c) Cross-sections of flowcell matrix.

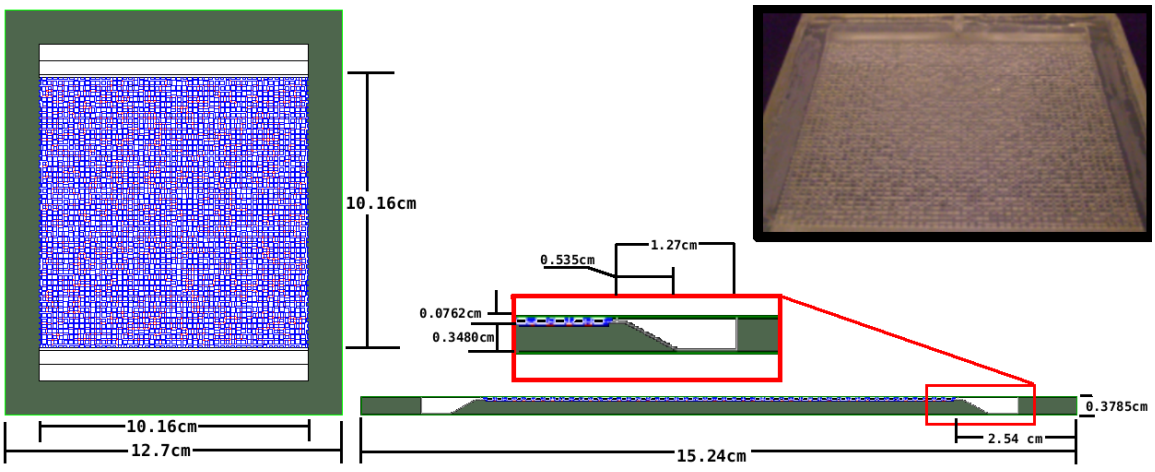

Figure 2: Flowcell dimensions and constructed flowcell.

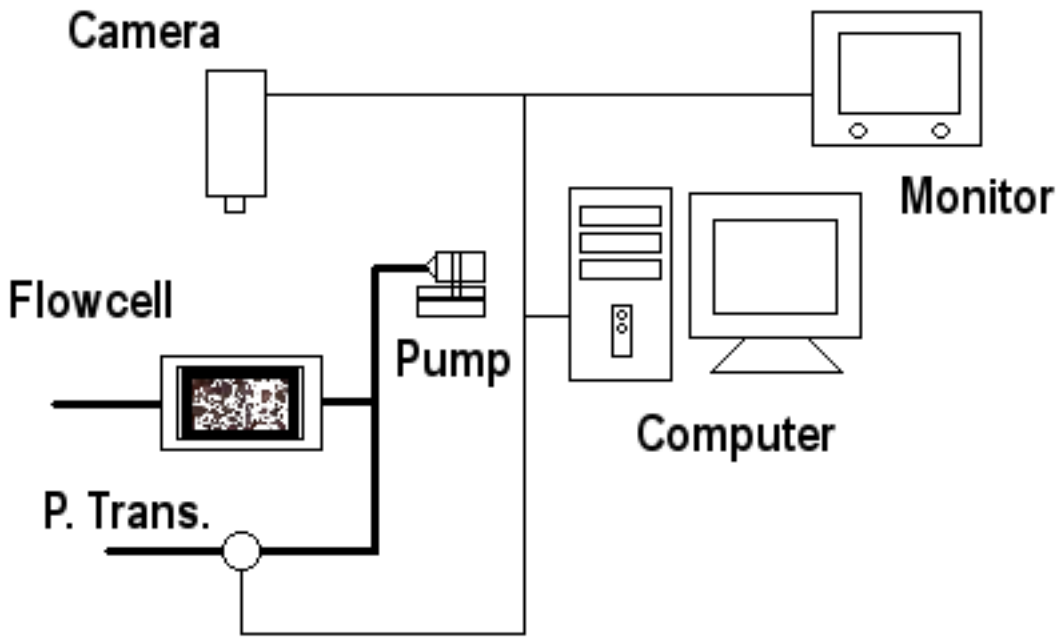

Figure 3: Schematic of experiment.

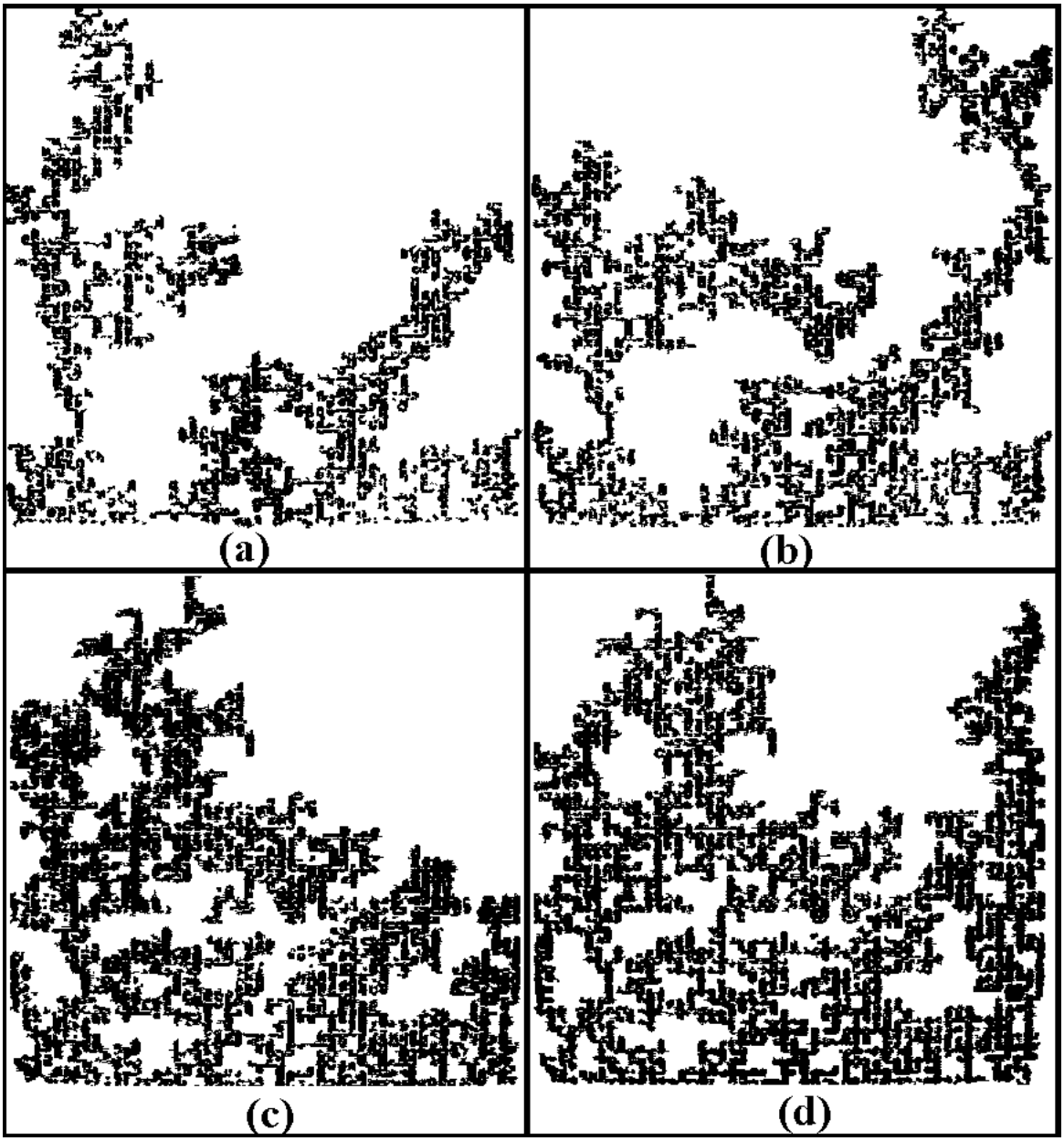

Figure 4: Final saturation of invading air, side 1 injection. Ca = (a) $9(10^{-4})$ (b) $2.3(10^{-4})$ (c) $2.3(10^{-5})$ (d) $2.3(10^{-6})$.

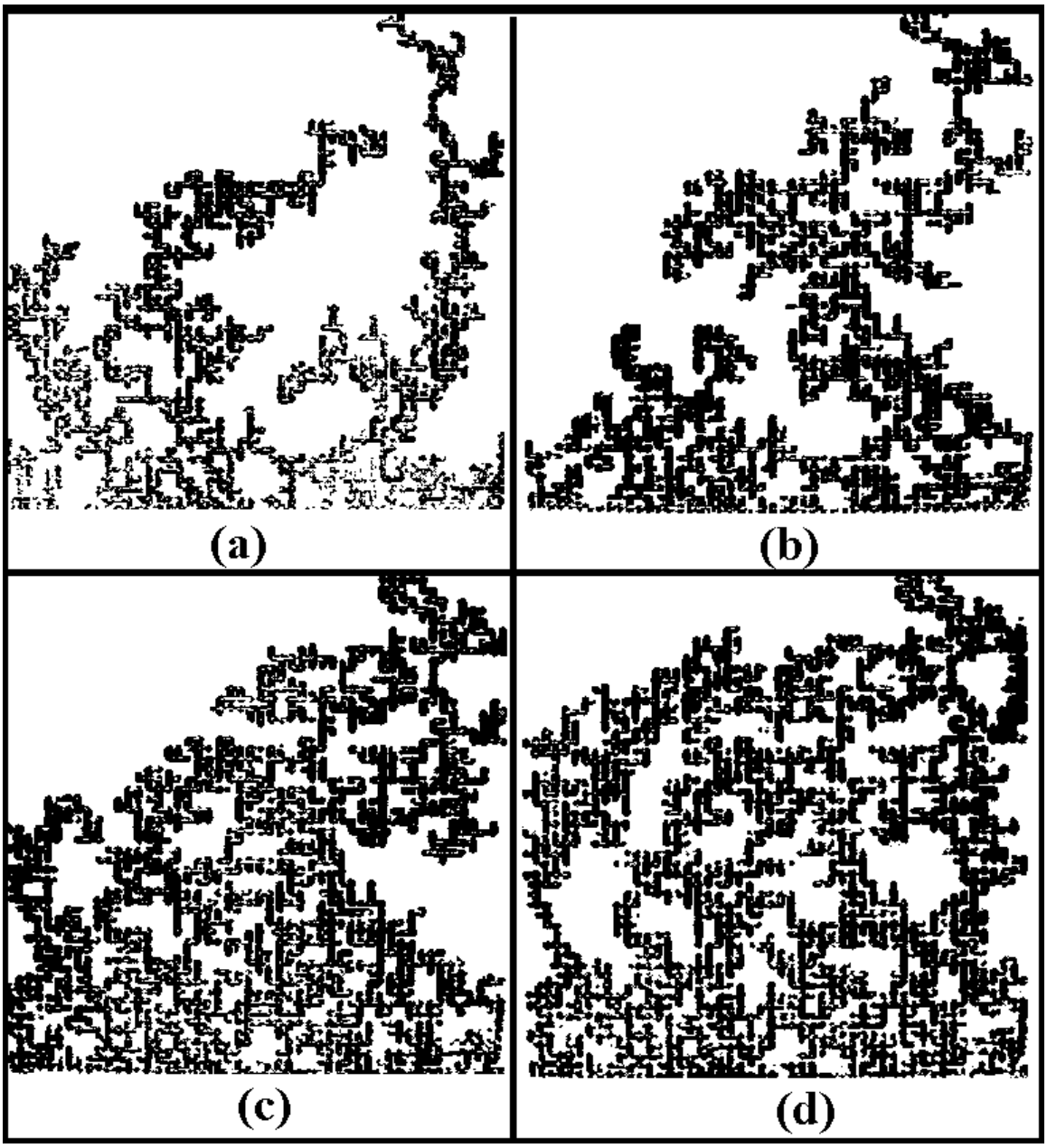

Figure 5: Final saturation of invading air, side 2 injection. Ca = (a) $9(10^{-4})$ (b) $2.3(10^{-4})$ (c) $2.3(10^{-5})$ (d) $2.3(10^{-6})$.

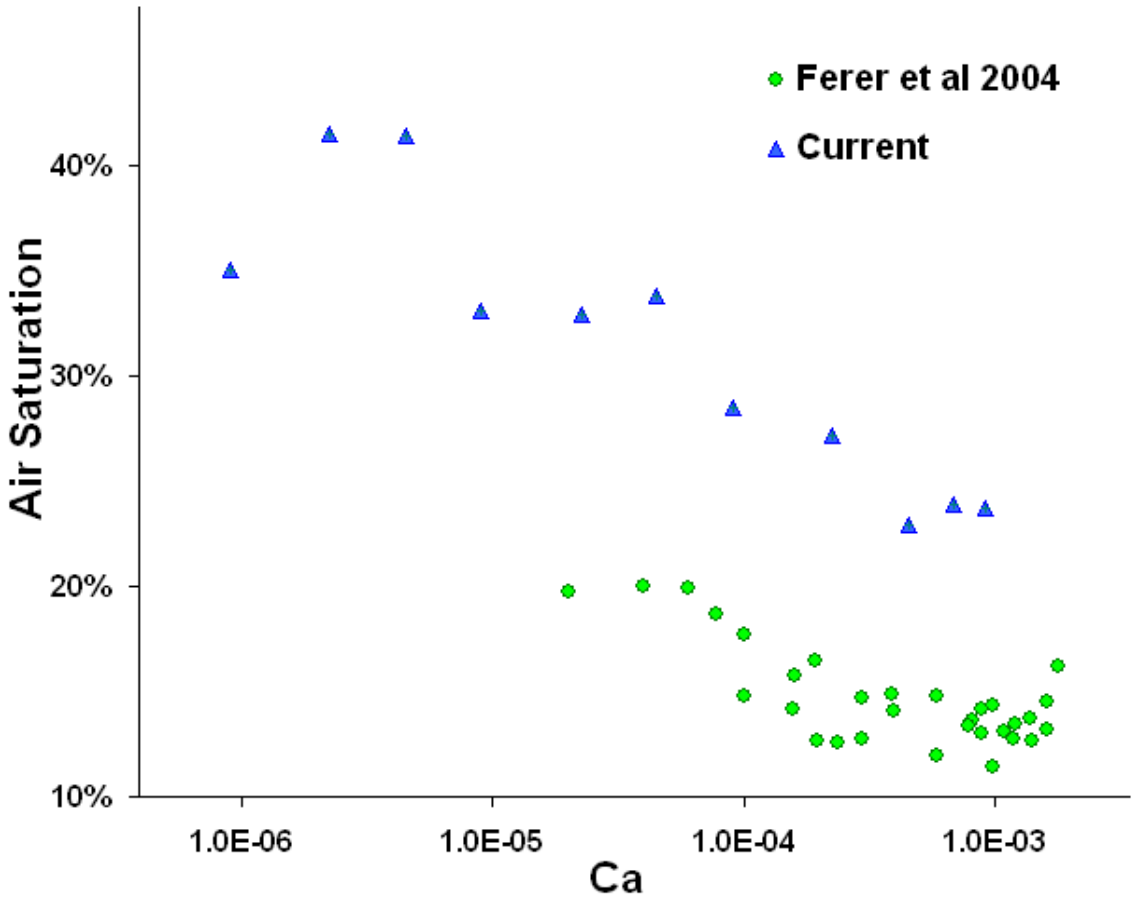

Figure 6: Percent saturation of invading air.

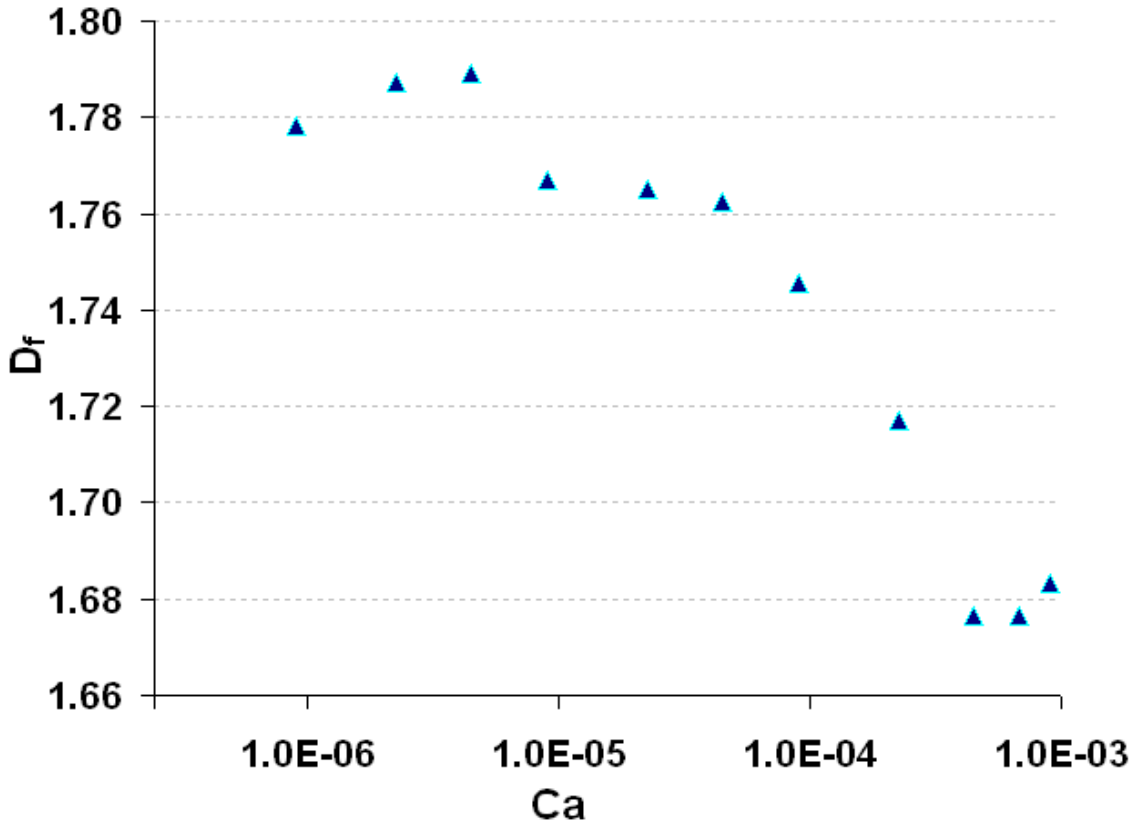

Figure 7: Fractal dimension of invading air mass.

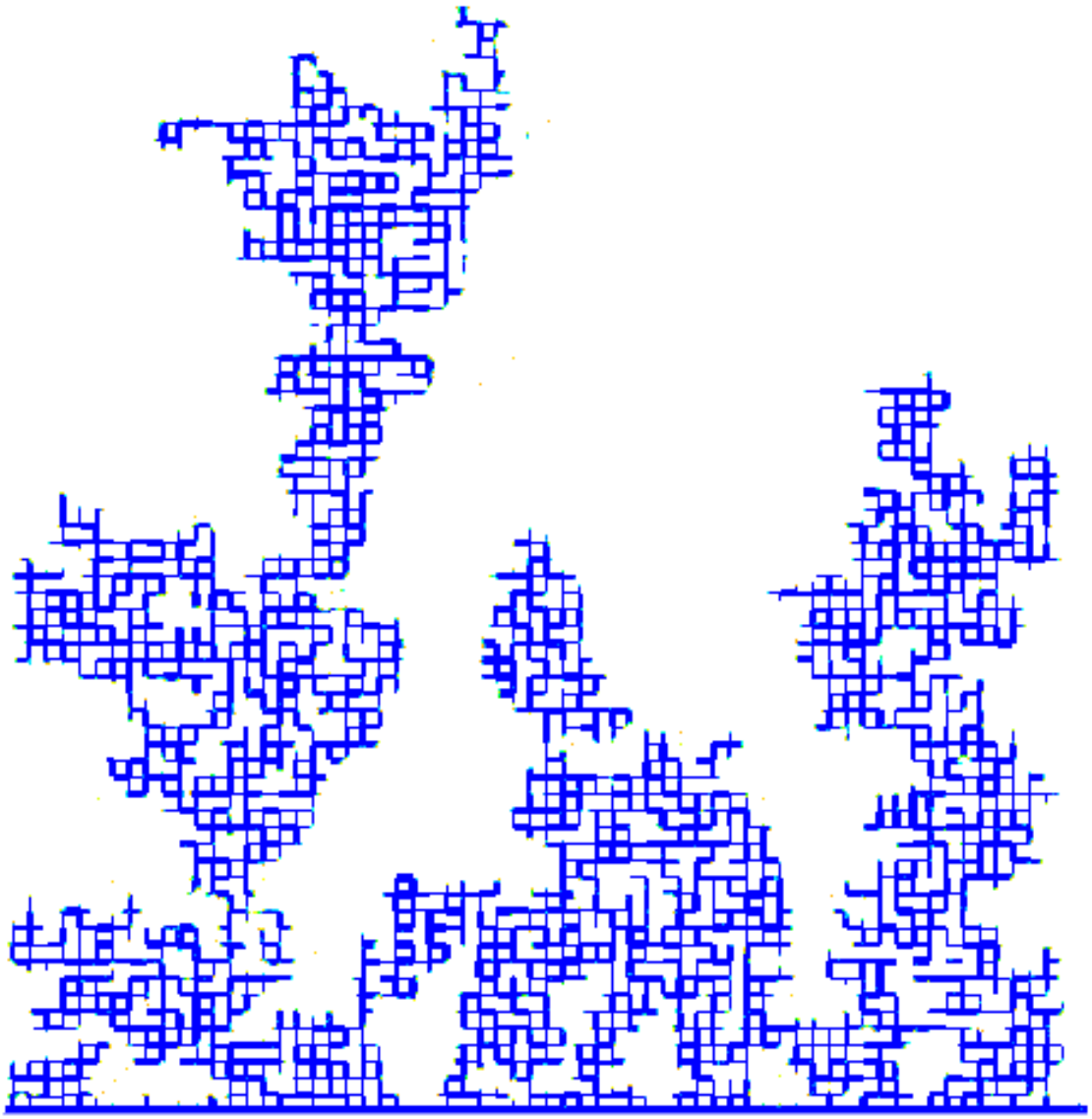

Figure 8: Numerical Saturation Profile. Air into Water, M = $1.8(10^{-2})$, = 72^{o} and Ca = $4.5(10^{-4})$.

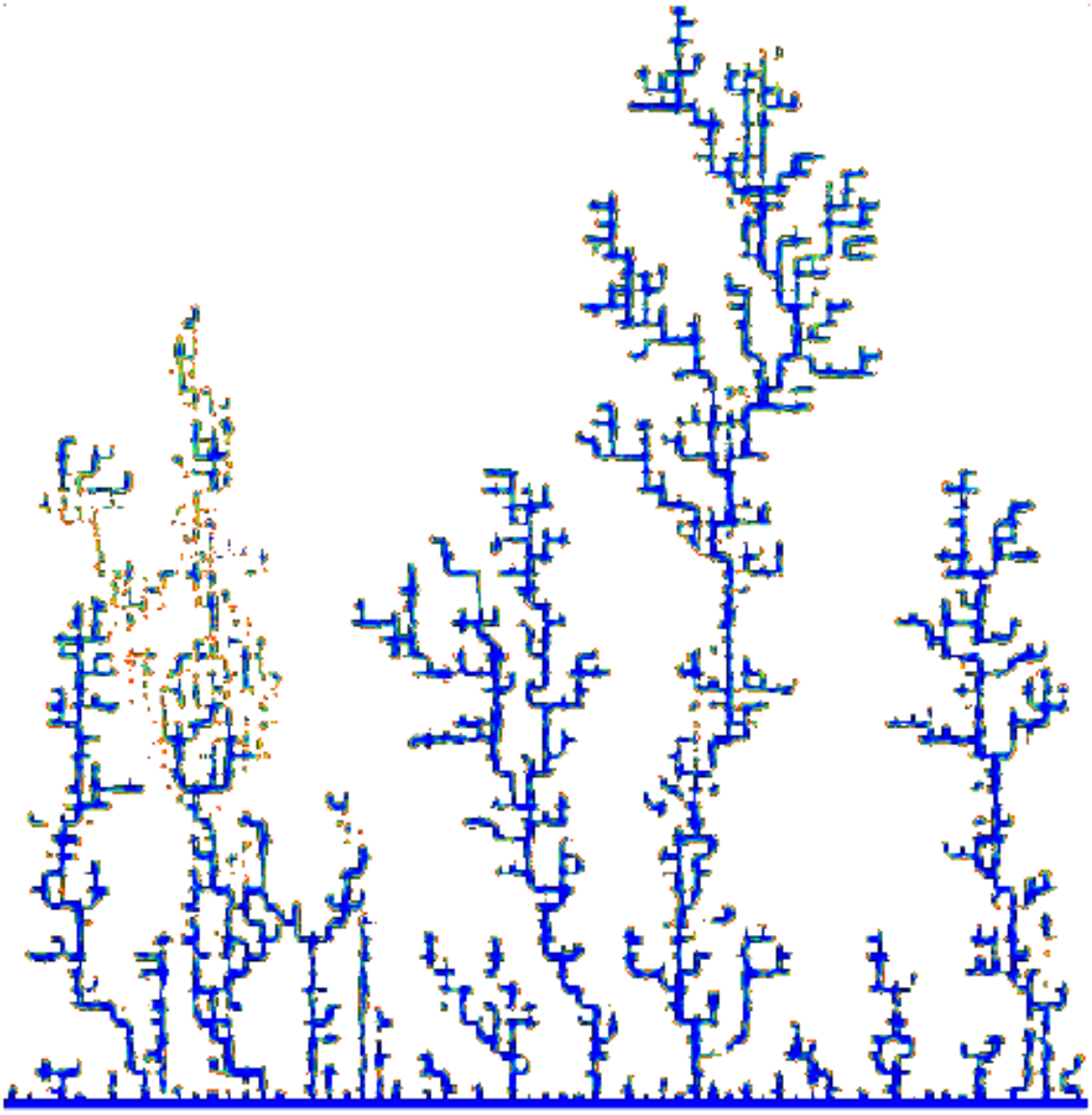

Figure 9:Numerical Saturation Profile. Air into Oil, M = $1.7(10^{-5})$, = 72^{o} and Ca = 0.98.